Localising individual atoms of tryptophan side chains in the metallo-β-lactamase IMP-1
by pseudocontact shifts from paramagnetic lanthanoid tags at multiple sites

Henry W. Orton,[a,*] Iresha D. Herath,[b,*] Ansis Maleckis,[c] Shereen Jabar,[b] Monika Szabo,[d] Bim Graham,[d] Colum Breen,[e] Lydia Topping,[e] Stephen J. Butler,[e] Gottfried Otting[a]

[a] ARC Centre of Excellence for Innovations in Peptide & Protein Science, Research School of Chemistry, Australian National University, Canberra, ACT 2601, Australia

[b] Research School of Chemistry, The Australian National University, Sullivans Creek Road, Canberra ACT 2601, Australia

[c] Latvian Institute of Organic Synthesis, Aizkraukles 21, LV-1006 Riga, Latvia

[d] Monash Institute of Pharmaceutical Sciences, Monash University, Parkville, VIC 3052, Australia

[e] Department of Chemistry, Loughborough University, Epinal Way, Loughborough, LE11 3TU, United Kingdom

Correspondence: Gottfried Otting (gottfried.otting@anu.edu.au)

[*] These authors contributed equally to this work.

Abstract

The metallo-β-lactamase IMP-1 features a flexible loop near the active site that assumes different conformations in single crystal structures, which may assist in substrate binding and enzymatic activity. To probe the position of this loop, we labelled the tryptophan residues of IMP-1 with 7-^{13}C-indole and the protein with lanthanoid tags at three different sites. The magnetic susceptibility anisotropy (Δχ) tensors were determined by measuring pseudocontact shifts (PCS) of backbone amide protons. The Δχ tensors were subsequently used to identify the atomic coordinates of the tryptophan side chains in the protein. The PCSs were sufficient to determine the location of Trp28, which is located in the active site loop targeted by our experiments, with high accuracy. Its average atomic coordinates showed barely significant changes in response to the inhibitor captopril. It was found that localisation spaces could be defined with better accuracy by including only the PCSs of a single paramagnetic lanthanoid ion for each tag and tagging site. The effect was attributed to the shallow angle with which

35 PCS isosurfaces tend to intersect if generated by tags and tagging sites that are identical except

36 for the paramagnetic lanthanoid ion.

37

1 Introduction

39 The metallo-β-lactamase IMP-1 is an enzyme that hydrolyses β-lactams, thus conferring

40 penicillin resistance to bacteria. First identified 30 years ago in the Gram-negative bacteria in

41 early 1990s from *Pseudomonas aeruginosa* and *Serratia marcescens* (Bush 2013), IMP-1 has

42 become a serious clinical problem due to horizontal gene transfer by a highly mobile gene

43 (bla_{IMP-1}) located on an integron (Arakawa et al., 1995), as the bla_{IMP-1} gene has been detected

44 in isolates of *Klebsiella pneumoniae*, *Pseudomonas putida*, *Alcaligenes xylosoxidans*,

45 *Acinetobacter junii*, *Providencia rettgeri*, *Acinetobacter baumannii* and *Enterobacter*

46 *aerogenes* (Ito et al., 1995; Laraki et al., 1999a; Watanabe et al., 1991). Critically, IMP-1

47 confers resistance also to recent generations of carbapenems and extended-spectrum

48 cephalosporins (Laraki et al., 199b; Bush et al., 2010; van Duin et al., 2013).

49   Multiple crystal structures have been solved of IMP-1, free and in complex with various

50 inhibitors (Concha et al., 2000; Toney et al., 2001; Moali et al., 2003; Hiraiwa et al., 2014;

51 Brem et al., 2016; Hinchliffe et al., 2016; 2018; Wachino et al., 2019; Rossi et al., 2021). IMP-

52 1 belongs to the subclass B1 of metallo-β-lactamases, which contain two zinc ions bridged by

53 the sulfur atom of a cysteine residue in the active site (Concha, 2000). One of Zn^{2+} ions can

54 readily be replaced by a Fe^{3+} ion (Carruthers et al., 2014). The active site is flanked by a loop

55 (referred to as L3 loop) that contains a highly solvent-exposed tryptophan residue surrounded

56 by glycine residues on either side. Both the loop and the tryptophan residue (Trp28 in the IMP-

57 1-specific numbering used by Concha et al. (2000) and Trp64 in the universal numbering

58 scheme by Galleni et al. (2001)) assume different conformations in different crystal structures,

59 suggesting that the loop acts as a mobile flap to cover bound substrate (Fig. 1A). The L3 loop

60 and the functional implication of its flexibility has been studied extensively for different

61 metallo-β-lactamases containing the Gly-Trp-Gly motif in the loop (Huntley et al., 2000; 2003;

62 Moali et al., 2003; Yamaguchi et al., 2015; Palacios et al., 2019; Gianquinto et al., 2020; Softley

63 et al., 2020). Flexibility of the L3 loop is a general feature also of many metallo-β-lactamases

64 without the Gly-Trp-Gly motif and is thought to contribute to the wide range of β-lactam

65 substrates that can be hydrolyzed by the enzymes (González et al., 2016; Linciano et al., 2019;

66 Salimraj et al., 2018). In the case of the metallo-β-lactamase from *B. fragilis*, which is closely

67 related to IMP-1, electron density could be detected for the Gly-Trp-Gly motif in the crystal

68 structure of the protein in the presence (Payne et al., 2003) but not absence of an inhibitor
69 (Concha et al., 1996), and an NMR relaxation study in solution confirmed the increased
70 flexibility of both the L3 loop and, in particular, the sidechain of the tryptophan residue
71 (Huntley et al., 2000). A similar situation prevails in the case of the IMP-1 variant IMP-13,
72 where different crystal structures of the ligand-free protein show the L3 loop in very different
73 conformations, sometimes lacking electron density, while NMR relaxation measurements
74 confirmed the increased flexibility of the loop (Softley et al., 2020).

75   Due to the rigidity of their sidechains, tryptophan residues frequently contribute to the
76 structural stability of three-dimensional protein folds and it is unusual to observe tryptophan
77 sidechains fully solvent-exposed as in the Gly-Trp-Gly motif of substrate-free IMP-1. The
78 functional role of Trp28 in IMP-1 was assessed in an early mutation study by mutating Trp28
79 to alanine and, in a different experiment, eliminating the L3 loop altogether. Enzymatic activity
80 measurements revealed an increase in the Michaelis constant K_m and a decrease in k_{cat}/K_m ratios
81 for all β-lactams tested, illustrating the importance of the Trp28 sidechain for catalytic activity.
82 Complete removal of the L3 loop reduced the k_{cat}/K_m ratios even further, but without
83 completely abolishing the enzymatic activity (Moali et al., 2003).

84

85

86
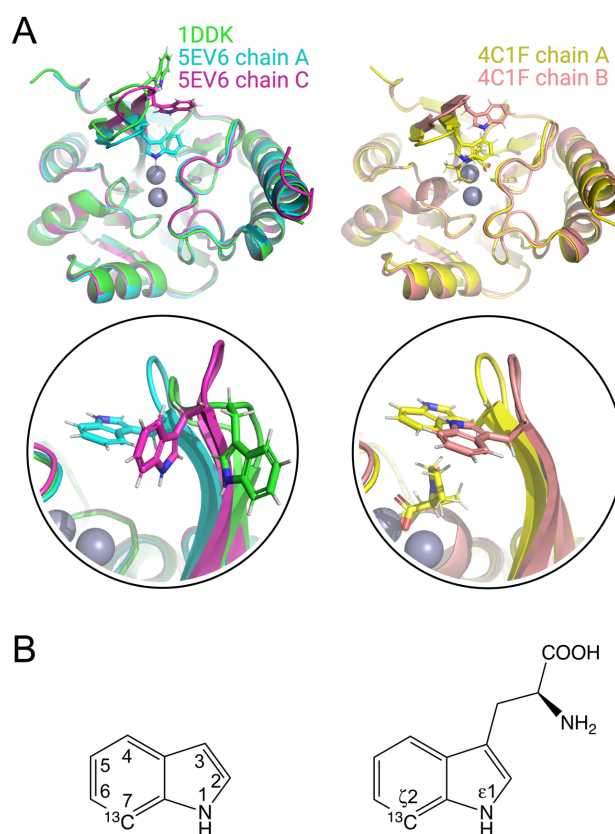
Figure 1. Crystal structures of IMP-1 with different conformations of the loop L3 and chemical structures of indole and tryptophan with atom names. (A) Superimposition of crystal structures of IMP-1 highlighting structural variations of Trp28 and the associated loop L3. The structures shown are of the Zn^{2+}/Zn^{2+} complex without inhibitor (green, PDB ID 1DDK, Concha et al., 2000; cyan for chain A and magenta for chain C, PDB ID 5EV6, Hinchliffe et al., 2016), with bound L-captopril (yellow for chain A and salmon for chain B, PDB ID 4CIF, Brem et al., 2016). Zn^{2+} ions are represented by grey spheres and bound captopril is shown in the structure 4C1F chain A. (B) Chemical structures of indole and tryptophan with selected ring positions labelled according to IUPAC conventions. The present work used indole synthesised with a ^{13}C-^{1}H group in position 7 and deuterium in the ring positions 2, 3, 4, 5 and 6 (Maleckis et al., 2021).

In the crystalline state, the conformation of a solvent-exposed loop is easily impacted by crystal packing forces. Therefore, it is unclear what the actual conformation of the L3 loop is in solution. To address this question, we used solution NMR spectroscopy to assess the location of Trp28 in IMP-1 both in the absence and presence of the inhibitor L-captopril, which inhibits metallo-β-lactamases by binding to the active-site zinc ions (Brem et al., 2016). The analysis was hindered by incomplete backbone resonance assignments of IMP-1 attributed to conformational exchange processes in parts of the protein (Carruthers et al., 2014). As it is difficult to accurately position the atoms of a solvent-exposed polypeptide loop in solution by nuclear Overhauser effects (NOE), we used pseudocontact shifts (PCS) generated by lanthanoid ions attached at different sites of IMP-1 to determine the location of Trp28 relative to the core of the protein. PCSs generated by multiple different paramagnetic metal ions or the same metal ion attached at different sites of a protein have previously been shown to allow localising atoms at remote sites of interest, such as in specific amino acid side chains (Pearce et al., 2017; Lescanne et al., 2018), bound ligand molecules (Guan et al., 2013; Chen et al., 2016) or proteins (Pintacuda et al., 2006; Keizers et al., 2010; de la Cruz et al., 2011; Kobashigawa et al., 2012; Brewer et al., 2015) or for 3D structure determinations of proteins (Yagi et al., 2013; Crick et al., 2015; Pilla et al., 2017).

IMP-1 contains six tryptophan residues, each containing several aromatic hydrogens with similar chemical shifts. To increase the spectral resolution in the 2D NMR spectra recorded for PCS measurements, we labelled each tryptophan sidechain with a single ^{13}C atom by expressing the protein in the presence of 7-^{13}C-indole (Fig. 1B; Maleckis et al., 2021). The

120 results show that the localisation spaces defined by the tryptophan PCSs fully agree with
121 previously determined crystal structures of IMP-1 for all tryptophan residues. They suggest
122 little change in the average conformation of the L3 loop upon binding of captopril. The results
123 illustrate the accuracy with which the positions of individual atoms can be determined by PCSs
124 from lanthanoid tags even in proteins of limited stability.
125
126 **2 Experimental procedures**
127 **2.1 Production, purification and tagging of proteins**
128 **2.1.1 Plasmid constructs and ^{13}C-labelled indole**
129 Three different cysteine mutations (A53C, N172C and S204C) were introduced into the bla_{IMP1}
130 gene in the pET-47b(+) plasmid using a modified QuikChange protocol (Qi and Otting, 2019).
131 Deuterated 7-^{13}C-indole was synthesized as described with deuteration in all positions other
132 than position 7 (Maleckis et al., 2021). The amino acid sequence of the protein was that
133 reported in the crystal structure 4UAM (Carruthers et al., 2014), except that the N-terminal
134 alanine residue was substituted by a methionine to avoid heterogeneity by incomplete
135 processing by amino peptidase.
136
137 **2.1.2 Protein production**
138 Uniformly ^{15}N-labelled samples of the cysteine mutants of IMP-1 were expressed in *E. coli*
139 BL21(DE3) cells. The cells were grown at 37 °C in Luria–Bertani (LB) medium containing 50
140 mgL^{-1} kanamycin until the OD$_{600}$ reached 0.6–0.8 and were then transferred to 300 mL of M9
141 medium (6 gL^{-1} Na$_2$HPO$_4$, 3 gL^{-1} KH$_2$PO$_4$, 0.5 gL^{-1} NaCl, pH 7.2) supplemented with 1 gL^{-1}
142 of ^{15}NH$_4$Cl. After induction with isopropyl-β-D-thiogalactopyranoside (IPTG, final
143 concentration 1 mM), the cells were incubated at room temperature for 16 hours. Following
144 centrifugation, the cells were resuspended in buffer A (50 mM HEPES, pH 7.5, 100 μM ZnSO$_4$)
145 for lysis by a homogeniser (Avestin Emulsiflex C5). The supernatant of the centrifuged cell
146 lysate was loaded onto a 5 mL SP column, the column was washed with 20 column volumes
147 buffer B (same as buffer A but with 50 mM NaCl) and the protein was eluted with a gradient
148 of buffer C (same as buffer A but with 1 M NaCl).
149 IMP-1 samples containing 7-^{13}C-tryptophan were produced by continuous exchange
150 cell-free protein synthesis (CFPS) from PCR-amplified DNA with eight-nucleotide single-
151 stranded overhangs as described (Wu et al., 2007), using 7-^{13}C-indole as a precursor for the *in*
152 *vitro* production of tryptophan (Maleckis et al., 2021). The CFPS reactions were conducted at
153 30 °C for 16 h using 1 mL inner reaction mixture and 10 mL outer buffer. Tryptophan was

154   omitted from the mixture of amino acids provided and deuterated 7-^{13}C-indole was added from

155   a stock solution in 50 % DMSO/50 % H$_2$O to the inner and outer buffers at a final concentration

156   of 0.75 mM. The protein samples were purified as described above. About 5 mg of the indole

157   was required for preparing each NMR sample.

158

159   **2.1.3 Ligation with C2-Ln^{3+} tag**

160   To ensure the reduced state of cysteine thiol groups, the protein samples were treated with 2

161   mM dithiothreitol (DTT) for 1 hour. Subsequently, the DTT was removed using an Amicon

162   ultrafiltration centrifugal tube with a molecular weight cut-off of 10 kDa, concentrating the

163   protein samples to 50 μM in buffer A. The samples were incubated overnight at room

164   temperature with shaking in the presence of five-fold molar excess of C2 tag (Graham et al.,

165   2011; de la Cruz et al., 2011) loaded with either Y^{3+}, Tb^{3+} or Tm^{3+}. Following the tagging

166   reaction, the samples were washed using an Amicon centrifugal filter unit to remove unbound

167   tag and the buffer was exchanged to NMR buffer (20 mM MES, pH 6.5, 100 mM NaCl).

168

169   **2.1.4 Ligation with C12-Ln^{3+} tag**

170   The ligation reaction of IMP-1 N172C with the C12-Ln^{3+} tag loaded with either Y^{3+}, Tb^{3+} or

171   Tm^{3+} (Herath et al., 2021) was conducted in the same way as with the C2-Ln^{3+} tags, except that

172   the reactions were carried out in buffer A with the pH adjusted to 7.0.

173

174   **2.2 NMR spectroscopy**

175   All NMR data were acquired at 37 °C on Bruker 600 and 800 MHz NMR spectrometers

176   equipped with TCI cryoprobes designed for 5 mm NMR tubes, but only 3 mm NMR tubes were

177   used in this project. Protein concentrations were 0.6 mM and 0.2 mM for ^{15}N-HSQC spectra

178   of samples labelled with the C2 and C12 tag, respectively. The protein concentrations were 0.4

179   mM for ^{13}C-HSQC and NOE-relayed ^{13}C-HSQC spectra. ^{15}N-HSQC spectra were recorded at

180   a ^{1}H-NMR frequency of 800 MHz with t_{1max} = 40 ms, t_{2max} = 170 ms, using a total recording

181   time of 3 h per spectrum. ^{13}C-HSQC spectra were recorded with a S^{3}E filter to select the low-

182   field doublet component due to the $^1J_{HC}$ coupling of the ^{13}C-labelled tryptophan side chains.

183   The pulse sequence is shown in Fig. S9 and the spectra were recorded at a ^{1}H-NMR frequency

184   of 600 MHz using t_{1max} = 20–50 ms, t_{2max} = 106 ms and total recording times of 2 h per

185   spectrum. ^{13}C-HSQC spectra with NOE relay were recorded without decoupling in the ^{13}C-

186   dimension, relying on relaxation and ^{13}C equilibrium magnetisation to emphasize the narrow

187 doublet component. The NOE mixing time was 150 ms and the total recording time 3 h per
188 spectrum. The pulse sequence is shown in Fig. S10.

189   To account for uncertainties in concentration measurements, samples with L-captopril
190 were prepared with a nominal ratio of captopril to protein of 1.5:1. In the case of samples
191 tagged with the C2 tag, however, this lead to gradual release of some of the tag, as captopril
192 contains a free thiol group and the disulfide linkage of the C2 tag is sensitive to chemical
193 reduction. To limit this mode of sample degradation, the NOE-relayed $[^{13}C,^1H]$-HSQC spectra
194 were recorded with a smaller excess of captopril.

195

196 **2.3 $\Delta\chi$-tensor fits**

197 The experimental PCSs ($\Delta\delta^{PCS}$) were measured in ppm as the amide proton chemical shift
198 observed in NMR spectra recorded for the IMP-1 mutants A53C, N172C and S204C tagged
199 with Tm^{3+} or Tb^{3+} tags minus the corresponding chemical shift measured of samples made with
200 Y^{3+} tags. The resonance assignments of the wild-type Zn_2 enzyme (BMRB entry 25063) were
201 used to assign the ^{15}N-HSQC cross-peaks in the diamagnetic state. The program Paramagpy
202 (Orton et al., 2020) was used to fit magnetic susceptibility anisotropy ($\Delta\chi$) tensors to crystal
203 structures of IMP-1 solved in the absence and presence of the inhibitor captopril.

204

205 **3 Results**

206 **3.1 Protein production**

207 Three cysteine mutants of uniformly ^{15}N-labelled IMP-1 were produced *in vivo*, where cysteine
208 residues replaced Ala53, Asn172 and Ser204, respectively. The purified proteins were tagged
209 with C2 tags containing Tb^{3+} or Tm^{3+} as the paramagnetic ions and Y^{3+} as the diamagnetic
210 reference. Samples of the uniformly ^{15}N-labelled mutant N172C were also ligated with C12
211 tags containing the same set of metal ions. The chemical structures of the tags are depicted in
212 Fig. S1. To record ^{13}C-^1H correlation spectra of the tryptophan side chains with minimal
213 spectral overlap, additional samples of the cysteine mutants were produced with selectively
214 ^{13}C-labelled tryptophan residues. These samples were produced by cell-free protein synthesis
215 in the presence of 7-^{13}C indole, deuterated except at the 7 position, with the omission of
216 tryptophan, using a recently established protocol (Maleckis et al., 2021). The residual activity
217 of tryptophan synthase in the cell-free extract was sufficient to produce tryptophan from the
218 added ^{13}C-labelled indole. The resulting tryptophan residues contained a ^{13}C-^1H group in
219 position 7 ($^{13}C^{\zeta 2}$ and $^1H^{\zeta 2}$ in IUPAC nomenclature; Markley et al., 1998) and deuterons at all

other hydrogen positions of the indole ring except for the H^N atom ($H^{\varepsilon 1}$ in IUPAC nomenclature). The cell-free expression yielded about 2 mg of purified protein per millilitre of inner cell-free reaction mixture. Mass spectrometry indicated that the tryptophan residues of IMP-1 were $^{13}C/^2H$-labelled with about 80 % labelling efficiency at each of the six tryptophan positions (Fig. S2). The purified proteins were ligated with C2-Ln^{3+} tags containing either Tb^{3+}, Tm^{3+} or Y^{3+} as in the case of the ^{15}N-labelled samples. Ligation yields with the C2 tags were practically complete as indicated by mass spectrometry (Fig. S2). The ligation yield of the N172C mutant with C12 tags was about 90 % (Herath et al., 2021).

3.2 NMR experiments and resonance assignments

[^{15}N,^1H]-HSQC spectra were measured of the tagged proteins in the free state and in the presence of L-captopril (Fig. S3–S8). ^1H PCSs of backbone amide protons measured in these spectra were used to establish the $\Delta\chi$ tensors relative to the protein. The resonance assignment of the [^{15}N,^1H]-HSQC spectra in the presence of inhibitor was transferred from the corresponding spectra recorded in the absence of inhibitor. As no resonance assignments could reliably be made in this way in areas of spectral overlap, fewer resonance assignments were available in the presence than absence of inhibitor. Furthermore, due to captopril releasing some of the C2 tags from the protein by breaking the disulfide bridge of the tag attachment, spectra recorded in the presence of captopril contained additional cross-peaks from diamagnetic protein.

To obtain tagged protein that is inert against chemical reduction, we also attached the C12 tag to the mutant N172C. This tag, however, caused the appearance of additional peaks in the [^{15}N,^1H]-HSQC spectra (Fig. S7). The additional peaks appeared in different sample preparations, indicating sample degradation or perturbation of the local protein structure by the tag. We therefore based the rest of the work mainly on the PCSs obtained with the C2 tags. Tables S1 and S2 list the PCSs of the backbone amides measured in the absence and presence of captopril.

^1H PCSs of the tryptophan $H^{\zeta 2}$ protons were measured in [^{13}C,^1H]-HSQC spectra recorded with S^3E spin-state selection element (Meissner et al., 1997) in the ^{13}C dimension to select the slowly relaxing components of the doublets split by $^1J_{HC}$ couplings. Cross-peaks were observed for all six tryptophan residues except for the mutant N172C, which displayed cross-peaks of only five tryptophan indoles (Fig. 2). The missing signal was attributed to Trp176 because of its close proximity to the tagging site. The indole $H^{\varepsilon 1}$ proton is located within 2.9 Å

of the $H^{\zeta 2}$ proton and the NOE between both protons was readily observed in a $[^{13}C,^{1}H]$-HSQC experiment with NOE relay (Fig. 2). The $H^{\varepsilon 1}$ chemical shifts afforded better spectral resolution than the $H^{\zeta 2}$ resonances. Comparison of the predicted and observed PCSs yielded resonance assignments of all tryptophan $H^{\varepsilon 1}$ cross-peaks with particular clarity in the NOE-relayed $[^{13}C,^{1}H]$-HSQC spectrum (Fig. 2). In addition, the assignment was supported by paramagnetic relaxation enhancements (for example, Trp88 is near residue 53 and therefore its cross-peaks were strongly attenuated in the paramagnetic samples of the A53C mutant). Different PCSs were observed for all six tryptophan sidechains and different PCSs were observed for the $H^{\zeta 2}$ and $H^{\varepsilon 1}$ protons within the same indole sidechain. Each of the tryptophan sidechains showed PCSs in most, if not all, of the mutants. As the L3 loop is near residue 172, the mutant N172C endowed Trp28 with particularly large PCSs. Tables S3 and S4 report the PCSs measured in this way for the samples labelled with C2 tags.

In contrast, assigning the indole N-H groups in the $[^{15}N,^{1}H]$-HSQC spectra was much more difficult because IMP-1 is a protein prone to showing more than a single peak per proton (Figs S5 and S6). In particular, the $[^{15}N,^{1}H]$-HSQC spectrum of wild-type IMP-1 selectively labelled with ^{15}N-tryptophan displayed six intense and at least three weak $N^{\varepsilon 1}$–$H^{\varepsilon 1}$ cross-peaks (Fig. S6; Carruthers et al., 2014) and the $[^{15}N,^{1}H]$-HSQC spectra of the tagged cysteine mutants showed evidence of heterogeneity too (Fig. S5). Nonetheless, the six most intense $N^{\varepsilon 1}$–$H^{\varepsilon 1}$ cross-peaks could be assigned by comparison to the PCSs observed in the NOE-relayed $[^{13}C,^{1}H]$-HSQC spectrum and this assignment was used to measure the PCSs of the tryptophan $H^{\varepsilon 1}$ resonances in the mutant N172C tagged with C12 tag (Fig. S8; Table S4).

Spectra recorded in the presence of L-captopril were very similar to those recorded without the inhibitor, except that some new, narrow C-H cross-peaks appeared in the $[^{13}C,^{1}H]$-HSQC spectra of the mutants A53C and S204C, which were suggestive of protein degradation (Fig. 3). We consequently used the better-resolved indole H^{N} cross-peaks to identify the correct parent C-H cross-peaks. The chemical shifts of the tryptophan sidechains changed very little in response to the presence of L-captopril, except for the ^{13}C-chemical shift of Trp28, which is nearest to the ligand binding site. The PCSs of the indole protons measured in the presence of the inhibitor are listed in Tables S5 and S6.

3.2 $\Delta\chi$-tensor fits

The $\Delta\chi$-tensor parameters were determined using the program Paramagpy (Orton et al., 2020), using all available ^{1}H PCSs measured of backbone amides. Comparing the $\Delta\chi$ tensor fits to the

286 crystal structures 5EV6 chains A and C (Hinchliffe et al., 2016) and 1DDK (Concha et al.,
287 2000) of the free protein, the chain A of the structure 5EV6 proved to produce the smallest Q
288 factor by a small margin (Fig. S11) and was used as the reference structure of the free protein
289 for the subsequent evaluation. Similarly, chain A of the co-crystal structure published with the
290 inhibitor L-captopril (PDB ID: 4C1F; Brem et al., 2016) on average delivered better fits than
291 chain B and was used as the reference structure for the NMR data recorded in the presence of
292 L-captopril. The $\Delta\chi$-tensor fits of each mutant and tag used a common metal position for the
293 data obtained with the Tb^{3+} and Tm^{3+} tags. The fits positioned the paramagnetic centres at
294 distances between 8.2 and 9.4 Å from the C^β atom of the tagged cysteine residues, which is
295 compatible with the chemical structure of the C2-tag. Figure 4 shows the correlations between
296 back-calculated and experimental PCSs and Table S7 reports the fitted $\Delta\chi$ tensor parameters.
297 Very similar Q factors were obtained when using the PCSs measured in the absence of inhibitor
298 to fit the $\Delta\chi$ tensor to the co-crystal structure 4C1F or the PCSs measured in the presence of
299 inhibitor to fit the $\Delta\chi$ tensor to the crystal structure of the free protein. This indicates that the
300 protein structure did not change very much in response to inhibitor binding. This conclusion
301 was also indicated by the similarity between the backbone PCSs observed with and without
302 inhibitor (Fig. S12).

303   The $\Delta\chi$ tensors obtained with the Tb^{3+} tags were larger than those obtained with the
304 Tm^{3+} tags, which is also reflected by the consistently larger PCSs observed in the ^{13}C-^1H
305 correlation spectra of Fig. 2 and 3. The fits of $\Delta\chi$ tensors to the protein backbone also yielded
306 better Q factors for PCSs generated by Tb^{3+} than Tm^{3+} ions. Therefore, we determined the
307 localisation spaces of the tryptophan sidechains in the first instance by using their ^1H PCSs
308 measured with Tb^{3+} tags only.

309
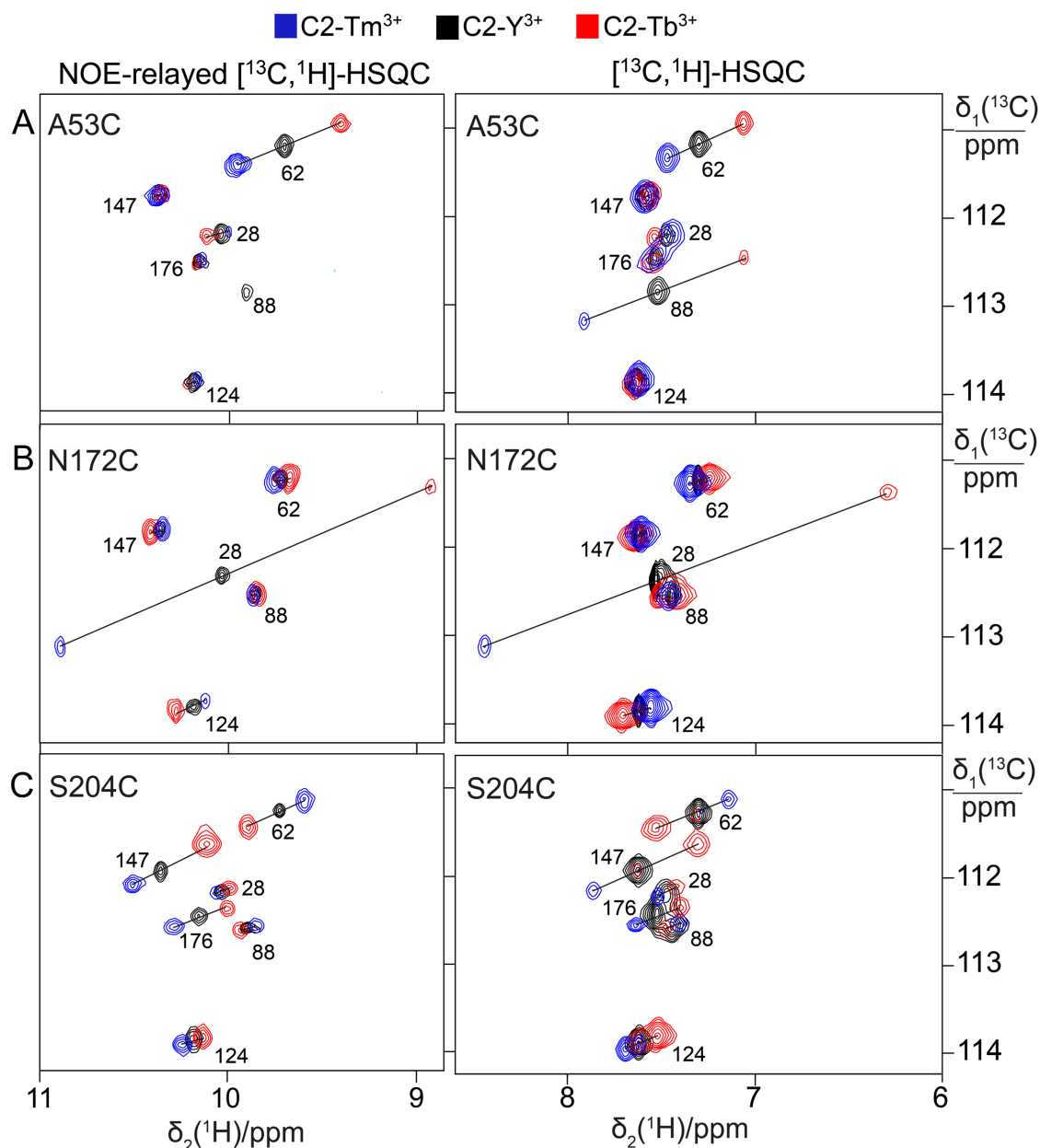
Figure 2. PCSs observed in ^{13}C-^1H correlation spectra of 0.4 mM solutions of IMP-1 mutants tagged with C2-Ln^{3+} tags and containing selectively isotope-labelled tryptophan produced from 7-^{13}C-indole deuterated in the positions 2, 4, 5 and 6. The plots show superimpositions of spectra recorded with diamagnetic (C2-Y^{3+}, black) or paramagnetic (C2-Tb^{3+}, red; C2-Tm^{3+}, blue) tags. All spectra were recorded with spin-state selection in the ^{13}C-dimension to record the narrow low-field component of each ^{13}C-doublet. Right panels: [^{13}C,^1H]-HSQC spectra. Left panels: NOE-relayed [^{13}C,^1H]-HSQC spectra (150 ms NOE mixing time) to record the H$^{\varepsilon 1}$ resonances of the tryptophan side chains. PCSs are indicated by lines connecting the peaks of paramagnetic and diamagnetic samples. The cross-peaks are assigned with the residue number of the individual tryptophan residues. (A) Mutant A53C. (B) Mutant N172C. (C) Mutant
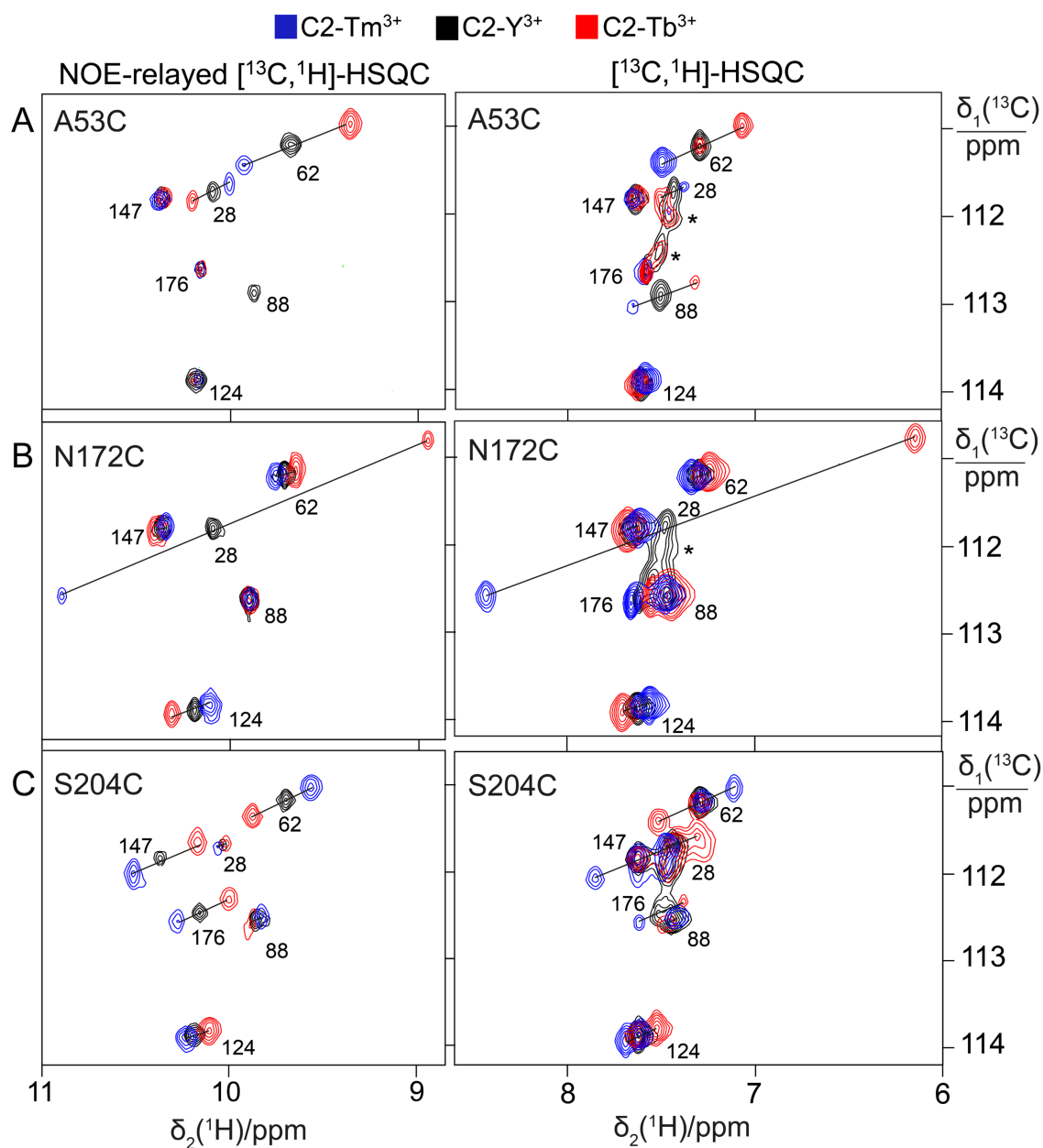
**Figure 3.** Effect of the presence of L-captopril on the PCSs observed in ^{13}C-^{1}H correlation spectra of 0.4 mM solutions of IMP-1 mutants. Protein preparations and experimental parameters were the same as in Fig. 2. Spectra recorded with diamagnetic (C2-Y^{3+}, black) or paramagnetic (C2-Tb^{3+}, red; C2-Tm^{3+}, blue) tags are superimposed. Right column: $[^{13}C,^{1}H]$-HSQC spectra. Left column: NOE-relayed $[^{13}C,^{1}H]$-HSQC spectra recorded with 150 ms NOE mixing time. Stars mark cross-peaks of species putatively attributed to protein degradation. (A) Mutant A53C. (B) Mutant N172C. (C) Mutant S204C.
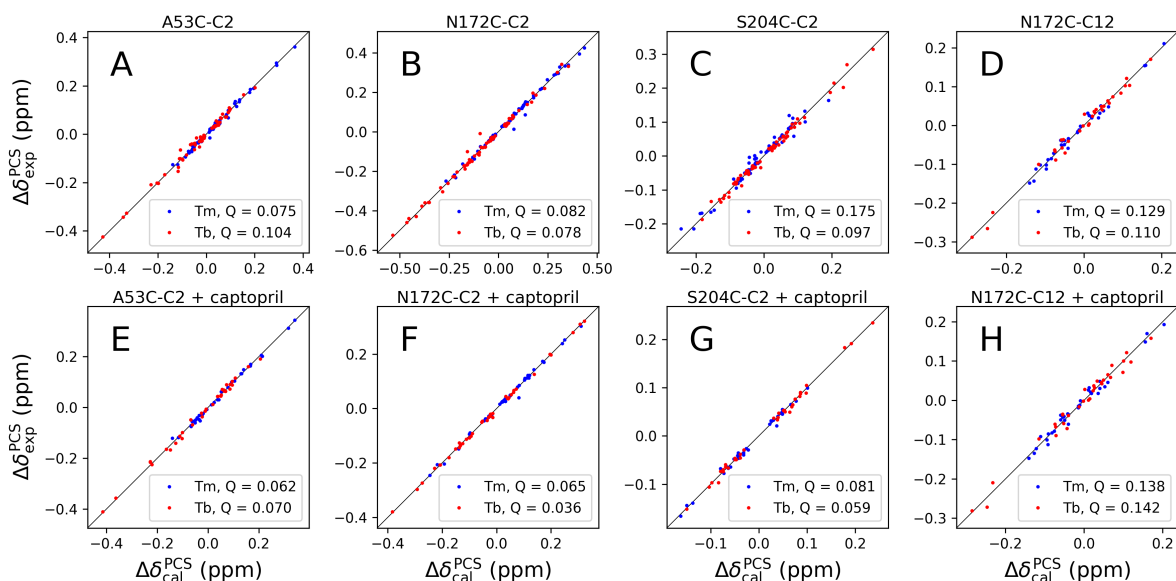
Figure 4. Correlations between back-calculated and experimental ^{1}H PCSs measured of backbone amides of IMP-1 with C2 tags at three different sites (positions 53, 172 and 204) and the C12 tag in position 172. Red and blue data points correspond to the PCS data obtained with Tb^{3+} and Tm^{3+} tags, respectively. (A) Mutant A53C with C2 tag. (B) Mutant N172C with C2 tag. (C) Mutant S204C with C2 tag. (D) Mutant N172C with C12 tag. (E) Same as (A) but in the presence of captopril. (F) Same as (B) but in the presence of captopril. (G) Same as (C) but in the presence of captopril. (H) Same as (D) but in the presence of captopril. PCS data in (A)–(D) were used to fit $\Delta\chi$ tensors to the structure 5EV6. PCS data in (E)–(F) were used to fit $\Delta\chi$ tensors to the structure 4C1F.

3.3 Determining the localisation spaces of tryptophan sidechains

The $\Delta\chi$ tensors determined of backbone amides not only enabled the resonance assignment of the tryptophan sidechains by comparing back-calculated with experimental PCSs, but also allowed translation of the indole PCSs into restraints that define the locations of the tryptophan H$^{\zeta 2}$ and H$^{\varepsilon 1}$ atoms with respect to the rest of the protein. The concept of localising nuclear spins by PCSs that are generated by lanthanoid tags at different sites is well-established (see, e.g., Yagi et al., 2013; Lescanne et al., 2018; Zimmermann et al., 2019). It can be visualised by representing each PCS restraint by the corresponding PCS isosurface, which comprises all points in space where this PCS value is generated by the $\Delta\chi$ tensor (Fig. 5). With PCS restraints from two different metal sites, the intersection between the respective isosurfaces defines a line. The intersection of this line with the PCS isosurface from a third $\Delta\chi$ tensor defines two points. While a fourth $\Delta\chi$ tensor could unambiguously produce a single solution, a fourth tensor

355 may not be required if one of these two points is incompatible with the covalent structure of

356 the protein. In favourable circumstances, the constraints imposed by the covalent structure may

357 even allow the accurate positioning of nuclear spins by PCSs generated from only two different

358 $\Delta\chi$ tensors (Pearce et al., 2017). Therefore, the present study was successful with only three

359 different tagging sites. Figure S13 illustrates the concept for the Trp28 $H^{\varepsilon 1}$ atom.

360   The spatial definition of the intersection point defined by the PCS isosurfaces depends

361 on the experimental uncertainties in a non-isotropic way, as the PCS isosurfaces rarely intersect

362 in an orthogonal manner and the PCS gradients differ for each $\Delta\chi$ tensor. To capture a

363 localisation space, which allows for the experimental uncertainty in the measured PCS data

364 and fitted $\Delta\chi$ tensors, we mapped the spatial field of root-mean-squared deviations (RMSD)

365 between experimental and calculated PCS values and defined the boundary of the localisation

366 space by a maximal RMSD value. In addition, uncertainties in the $\Delta\chi$ tensors were propagated

367 by averaging over the results from 20 $\Delta\chi$-tensor fits performed with random omission of 20 %

368 of the backbone PCS data. In the present work, the routine for defining the localisation space

369 was implemented as a script in the software Paramagpy (Orton et al., 2020). Figure 6 shows

370 the resulting localisation spaces for the $H^{\varepsilon 1}$ and $H^{\zeta 2}$ atoms of Trp28, using the PCS data

371 obtained for the three cysteine mutants A53C, N172C and S204C with the C2-Tb^{3+} tag as well

372 as the N172C mutant with the C12-Tb^{3+} tag.

373   The localisation spaces found for the $H^{\varepsilon 1}$ and $H^{\zeta 2}$ atoms of Trp28 were clearly different.

374 Furthermore, the distance between them corresponded closely to the distance expected from

375 the chemical structure of the indole ring (2.9 Å). The irregular shapes of the localisation spaces

376 displayed in Fig. 6 purely reflect the relative geometry of the intersecting PCS isosurfaces and

377 do not take into account any dynamic flexibility of the L3 loop or protein structure. In

378 particular, the relevant PCS isosurfaces associated with the C2 tag at sites N172C and S204C

379 intersect at a shallow angle, which leads to the elongated shape of the localisation space for the

380 Trp28 $H^{\zeta 2}$ atom (Fig. S13). For the nitrogen-bound $H^{\varepsilon 1}$ atom, the localisation space was

381 restricted further by the additional data obtained with the C12 tag at site N172C (Fig. 6).

382 Calculating the localisation spaces from the Tm^{3+} data yielded very similar results (Fig. S14).

383 The agreement of the localisation spaces of Trp28 with chain A of the previously published

384 crystal structure 5EV6 is excellent and they are clearly incompatible with the conformations

385 observed in chain C of the same structure or in the structure 1DDK (Fig. 1A).

386   Due to close proximity to the C2 tags in the N172C mutant, the largest PCSs were

387 observed for Trp28 $H^{\varepsilon 1}$ but, in the absence of captopril, their exact magnitude appeared about

388   0.3 ppm smaller in the [^{15}N,^{1}H]-HSQC (Fig. S5b) than the NOE-relayed [^{13}C,^{1}H]-HSQC (Fig.

389   2B) spectrum. The centre of the localisation space of Trp28 H$^{\epsilon1}$ moved to a slightly more open

390   L3 loop conformation when using the smaller PCS detected in the [^{15}N,^{1}H]-HSQC spectrum

391   of the N172C mutant labelled with the C2-Tb^{3+} tag. The space still encompassed the

392   coordinates observed in the structure 5EV6, limiting the significance of this difference in PCS.

393   None of the minor additional cross-peaks observed in any of the sample preparations

394   could be attributed to alternative conformations of Trp28 either. In particular, the most extreme

395   conformation observed in the crystal structure 1DDK (green in Fig. 1) predicts PCSs > 1 ppm

396   for Trp28 H$^{\epsilon1}$ in the mutant N172C with C2 tags, but we observed no PCS of this magnitude

397   for any of the unassigned peaks.

398

399

400   **3.4 Defining the localisation space with one versus two lanthanoid ions in the same tag**

401   **and at the same site**

402   Unexpectedly, determining separate localisation spaces from the Tm^{3+} and Tb^{3+} datasets

403   yielded more plausible results than when both datasets were used simultaneously. Careful

404   inspection showed that the close alignment of the $\Delta\chi$ tensors of the Tm^{3+} and Tb^{3+} data resulted

405   in particularly shallow intersection angles of the respective PCS isosurfaces. In calculating the

406   localisation space of Trp28, the PCS isosurfaces arising from the N172C mutant carried by far

407   the greatest weight as this site is closer to residue 28 than the sites 53 and 204. Therefore, the

408   Tm^{3+} and Tb^{3+} data from the N172C mutant dominated the PCS RMSD calculation and the

409   intersection between the associated isosurfaces pulled the final localisation space to a

410   structurally implausible location, which was unstable with respect to small perturbations in $\Delta\chi$-

411   tensor orientations associated with the tensors at site 172. In contrast, considering the Tm^{3+} and

412   Tb^{3+} datasets separately allowed the localisation spaces to be determined by the intersections

413   with PCS isosurfaces from the other sites. The resulting localisation spaces consistently were

414   compatible with crystal structures.

415

416
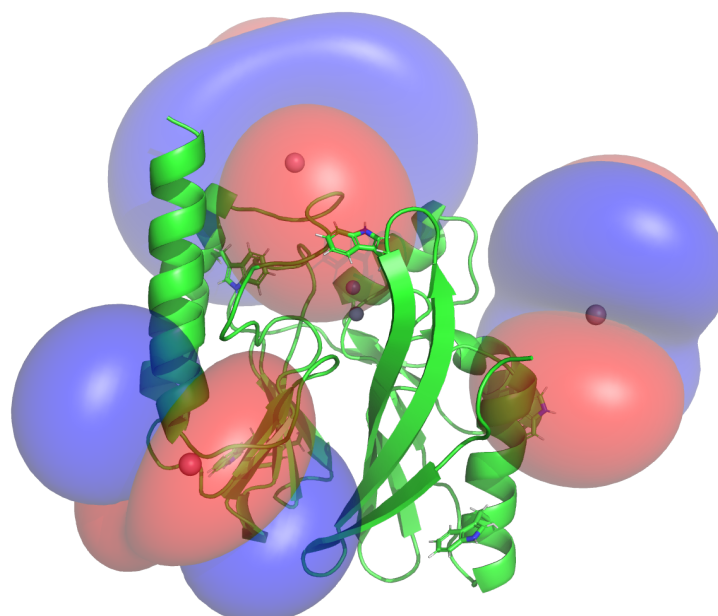
Figure 5. PCS isosurfaces of the IMP-1 mutants A53C, N172C and S204C plotted on the crystal structure 5EV6. The respective $\Delta\chi$ tensors were determined from the ^{1}H PCSs measured of backbone amides. Blue/red isosurfaces correspond to PCSs of +/-1.0 ppm, respectively, generated with C2-Tb^{3+} tags.

421

422
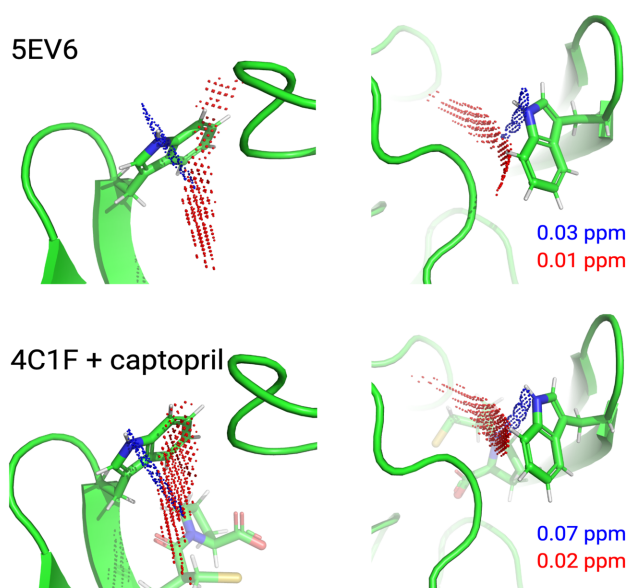
Figure 6. Localisation space of the sidechain of Trp28 defined by the PCSs from tags in the IMP-1 mutants A53C, N172C and S204C. The left and right panels display the same results in two different orientations. Red and blue points outline localisation spaces determined for the H$^{\zeta2}$ and H$^{\varepsilon1}$ atoms, respectively. The localisation space of the H$^{\zeta2}$ atom was defined by the PCSs and $\Delta\chi$ tensors determined for the Tb^{3+}-loaded C2 tags, while the localisation space of the H$^{\varepsilon1}$ atom was restricted by additional data obtained with C12-Tb^{3+} tag at site N172C. The

boundaries of the respective localisation spaces displayed are defined by the PCS RMSD values

indicated in ppm. The top panel depicts the localisation spaces determined for the free protein

plotted on chain A of the crystal structure 5EV6 depicted in two different orientations. The

lower panel depicts the localisation spaces determined in the presence of captopril plotted on

chain A of the crystal structure 4C1F.

3.5 L3 loop conformation in the presence of L-captopril

Figure 6 shows that, within the uncertainty of the experiments, the localisation space of the

indole sidechain of Trp28 is invariant with respect to the presence or absence of captopril.

Conservation of the L3 loop conformation with and without inhibitor is supported by the close

similarity in all the PCSs observed for Trp28 in the NOE-relayed $[^{13}C,^{1}H]$-HSQC spectra (Fig.

2 and 3). In the $[^{1}H,^{15}N]$-HSQC spectra of the mutant N172C with C2 tag, however, the PCSs

observed for Trp28 $H^{\varepsilon 1}$ appeared somewhat smaller without than with captopril (Fig. S5b). As

the PCSs of backbone amides were very similar in the absence and presence of the inhibitor

(Fig. S12), this difference in PCS suggests a change in L3 loop conformation, contradicting the

observations made with the selectively ^{13}C-labelled samples. As discussed above, using the

smaller PCS of Trp28 $H^{\varepsilon 1}$ did not sufficiently change its localisation space in the free protein

to render it incompatible with the coordinates of the structure 5EV6. Therefore, as far as the

data of the ^{15}N-labelled samples indicate a conformational change of the L3 loop between the

free and bound state, it is small. We attribute the differences in PCSs observed between the

selectively ^{13}C-labelled and uniformly ^{15}N-labelled samples to differences in sample

preparation of unknown origin, which are also reflected by different numbers of weak

unassigned cross-peaks (Figs 2, 3, S5 and S6).

The cross-peak intensities of the Trp28 sidechain resonances are relatively weak

compared with those of the other tryptophan sidechains, suggesting that Trp28 is subject to

dynamics that broaden its resonances. Its cross-peaks appeared slightly weaker in the presence

than in the absence of inhibitor (Fig. 2 and 3), suggesting a change in dynamics caused by the

inhibitor binding. Previous NMR studies of metallo-β-lactamases reported faster $R_2(^{15}N)$

relaxation rates of the L3-loop tryptophan sidechain in the presence than in the absence of

inhibitor, which was attributed to dampened dynamics (Huntley et al., 2000; Softley et al.,

2020). In the presence of dynamics, the localisation spaces determined in the present work

must be considered averages that do not report on the amplitude or direction of motions.

3.6 Localisation spaces of tryptophan side chains other than Trp28

As the tagging sites had been designed to analyse the conformation of the L3 loop, they were positioned at similar distances from the L3 loop and therefore not optimal for determining localisation spaces of the other tryptophan residues. Nonetheless, clear differences were observed in the PCSs of the $H^{\xi 2}$ and $H^{\epsilon 1}$ atoms (Fig. 2), allowing the separation of the respective localisation spaces, which also proved to be in excellent agreement with the conformations of the side-chain indoles of Trp62, Trp124 and Trp147 as found in the crystal structure (Fig. S15), whereas the data were insufficient to determine the sidechain conformation of Trp176.

4 Discussion

The L3 loop of metallo-β-lactamases is known to be flexible and, in the specific case of IMP-1, significantly assists in substrate binding and enzymatic activity (Moali et al., 2003). As the substrate is sandwiched between the di-zinc site and the L3 loop, it is tempting to think that the loop opens up for substrate binding and product release while it may be closed during the enzymatic reaction to hold the substrate and reaction intermediate in place. In contrast, some of the conformations observed in crystal structures of IMP-1 obtained in the presence and absence of the inhibitor L-captopril, revealed the loop in almost identical conformations (Brem et al., 2016). This observation is inconclusive, however, as the L3 loop forms more extensive intermolecular contacts with neighbouring protein molecules in the crystal lattice than intramolecular contacts. In addition, other crystal structures observed the loop to move by almost 3 Å in response to a different inhibitor (Concha et al., 2000). This prompted us to probe its actual location in the absence of crystal packing forces in solution, a task which is difficult to tackle by traditional NMR spectroscopic methods that rely on short-range NOEs.

Our results show that by furnishing IMP-1 with paramagnetic lanthanoid tags, the coordinates of the indole sidechain of Trp28, which is a key residue near the tip of the loop, can be determined with remarkable accuracy even in the free protein, where the available crystal structures position the L3 loop in a conformation without any direct contacts with the core of the protein. Indeed, the localisation space identified by the NMR data of the free protein proved to be sufficiently well-defined to discriminate between different crystal structures of IMP-1, as well as between different chains in the same asymmetric crystal unit. For example, the sidechain orientation of Trp28 observed in $[Fe^{3+},Zn^{2+}]$-IMP-1 (4UAM; Carruthers et al., 2014) proved to be in poor agreement with the PCS data, whereas the data were in full agreement with chain A in the structure 5EV6 of $[Zn^{2+},Zn^{2+}]$-IMP-1 without inhibitor

495   (Hinchliffe et al., 2016) and chain A in the structure 4C1F with bound L-captopril (Brem et al.,

496   2016). This highlights the outstanding capacity of PCSs to assess small conformational

497   differences.

498   The approach of using PCSs for local structure determination is particularly appealing

499   in the case of difficult proteins such as IMP-1, where the sequence-specific NMR resonance

500   assignments are incomplete due to line-broadening attributable to motions in the μs–ms time

501   range and additional signals are observed that either stem from protein degradation, misfolding

502   or alternative conformations in slow exchange with the main structure. Notably, all information

503   required to establish the $\Delta\chi$ tensors could be obtained from resolved cross-peaks observed in

504   sensitive [^{15}N,^{1}H]-HSQC spectra. Similarly, the localisation information of the tryptophan

505   sidechains could be obtained from sensitive ^{13}C-^{1}H and ^{15}N-^{1}H correlation spectra. Positioning

506   the lanthanoid tags relatively far from the substrate binding site avoided direct interference

507   with the binding loop structure.

508   In the face of additional signals from minor species, site-selective ^{13}C-labelling of the

509   tryptophan sidechains was particularly helpful for simplifying the [^{13}C,^{1}H]-HSQC spectra.

510   Gratifyingly, this could be achieved by providing suitably labelled indole without having to

511   synthesise the full amino acid (Maleckis et al., 2021).

512   It has been pointed out previously that the accuracy with which localisation spaces can

513   be determined is best when PCS isosurfaces intersect in an orthogonal manner (Pintacuda et

514   al., 2006; Lescanne et al., 2018; Zimmermann et al., 2019). In the present work, we found that,

515   counterintuitively, the provision of additional data can considerably degrade the accuracy of

516   the localisation space. This effect arises when PCS isosurfaces intersect at a shallow angle, as

517   the location of these intersections becomes very sensitive with regard to small errors in the

518   relative orientations of the underpinning $\Delta\chi$ tensors. Shallow intersection angles of PCS

519   isosurfaces are common, when two PCS datasets are from tags and tagging sites that differ only

520   in the identity of the paramagnetic metal ion in the tag. This situation commonly generates $\Delta\chi$

521   tensors of different magnitude and sign, but closely similar orientation (Bertini et al., 2001; Su

522   et al., 2008; Keizers et al., 2008; Man et al., 2010; Graham et al., 2011; Joss et al., 2018;

523   Zimmermann et al., 2019). Therefore, while the use of Tm^{3+} and Tb^{3+} tags is helpful for

524   assigning the cross-peaks in the paramagnetic state, more robust results are obtained by using

525   only one of these data sets for calculating the localisation space. Good localisation spaces were

526   thus obtained by using only PCSs measured for Tb^{3+} tags (Fig. 6) or only PCSs measured for

527   Tm^{3+} tags (Fig. S13). In contrast, however, very different tags attached at the same site, such

528 as the C2 and C12 tags installed in the mutant N172C, produced independent $\Delta\chi$-tensor

529 orientations and therefore contributed positively to localising the Trp28 H$^{\varepsilon 1}$ atom.

530   In principle it is inappropriate to explain a set of PCSs by a single $\Delta\chi$ tensor, if they are

531 generated by a lanthanoid tag attached via a flexible linker, which positions the lanthanide ions

532 at variable coordinates relative to the protein. In this situation, fitting a single $\Delta\chi$ tensor

533 amounts to an approximation. The effective $\Delta\chi$ tensors obtained in this way, however, can

534 fulfill the PCSs remarkably well (Shishmarev and Otting, 2013), as illustrated by the low Q

535 factors obtained in this work (Fig. 4), and the localisation spaces obtained for the tryptophan

536 sidechains are correspondingly well defined.

537   The accuracy, with which localisation spaces can be determined, further depends on the

538 accuracy with which PCSs can be measured (which critically depends on the reproducibility of

539 the sample conditions between the paramagnetic and diamagnetic states), the accuracy of the

540 protein structure used to fit the $\Delta\chi$ tensors and the angle with which PCS isosurfaces of different

541 tensors intersect. To take into account the uncertainties associated with the PCS isosurfaces, it

542 is useful to think of each of them individually as a shell of a certain thickness (rather than a

543 surface) that represents a compatible localisation space. Two shells of a given thickness share

544 a smaller common space if they intersect orthogonally than if they intersect at a shallow angle.

545   The present work employed ^{1}H PCSs only, although PCSs were also observed in the

546 indirect dimensions of the [^{13}C,^{1}H]-HSQC and [^{15}N,^{1}H]-HSQC spectra. We made this choice

547 because the paramagnetic tags give rise to weak molecular alignments in the magnetic field,

548 which result in residual anisotropic chemical shifts (RACS). The effect is unimportant for ^{1}H

549 spins but significant for nuclear spins with large chemical shift anisotropy (CSA) tensors such

550 as backbone nitrogens and aromatic carbons. Correcting for the RACS effect is possible with

551 prior knowledge of the CSA tensors and bond orientations (John et al., 2005). We therefore

552 chose not to measure PCSs of the heteronuclear spins in favour of improving sensitivity by

553 accepting a lower spectral resolution in the indirect dimensions.

554   Finally, the C12 tag was designed specifically with the intent to produce a more rigid

555 tether to the protein than the C2 tag, but this did not result in larger $\Delta\chi$ tensors (Table S7) and

556 the NMR spectra of IMP-1 N172C displayed more heterogeneity with the C12 than the C2 tag,

557 suggesting that the shorter and more rigid tether combined with the fairly high molecular

558 weight of the cyclen-lanthanoid complex may have perturbed the protein structure to some

559 degree.

560

5 Conclusion

The current work illustrates how $\Delta\chi$ tensors from paramagnetic lanthanoid ion tags installed at three different sites of the protein can be used to probe the conformation of a selected site in solution in unprecedented detail, provided the structure of most of the protein is known with high accuracy to allow fitting effective $\Delta\chi$ tensors of high predictive value. Importantly, however, the method is easily compromised, if two PCS isosurfaces intersect at a shallow angle as, in this situation, inaccuracies in $\Delta\chi$ tensor determinations have an outsized effect on positioning the localisation spaces defined by the PCSs. Therefore, improved results were obtained by not combining data from different metal ions bound to otherwise identical tags and tagging sites. In the present work, simplifying the NMR spectrum of tryptophan residues by site-selective isotope labelling proved to be of great value for sufficiently improving the spectral resolution to allow assigning the labelled resonances solely from PCSs and PREs. The strategy opens a path to detailed structural investigations of proteins of limited stability like IMP-1, for which complete assignments of the NMR spectrum are difficult to obtain.

598

599   **References**

600   Arakawa, Y., Murakami, M., Suzuki, K., Ito, H., Wacharotayankun, R., Ohsuka, S., Kato, N.,

601   and Ohta, M.: A novel integron-like element carrying the metallo-β-lactamase gene bla_{IMP},

602   Antimicrob. Agents Chemother., 39, 1612–1615, https://doi.org/10.1128/AAC.39.7.1612,

603   1995.

604   Bertini, I., Janik, M. B. L., Lee, Y. M., Luchinat, C., and Rosato, A.: Magnetic susceptibility

605   tensor anisotropies for a lanthanide ion series in a fixed protein matrix, J. Am. Chem. Soc.,

606   123, 4181–4188, https://doi.org/10.1021/ja0028626, 2001.

607   Brem, J., van Berkel, S. S., Zollman, D., Lee, S. Y., Gileadi, O., McHugh, P. J., Walsh, T. R.,

608   McDonough, M.A., and Schofield, C. J.: Structural basis of metallo-β-lactamase inhibition

609   by captopril stereoisomers, Antimicrob. Agents Chemother., 60, 142–150,

610   https://doi.org/10.1128/AAC.01335-15, 2016.

611   Brewer, K. D., Bacaj, T., Cavalli, A., Camilloni, C., Swarbrick, J. D., Liu, J., Zhou, A., Zhou,

612   P., Barlow, N., Xu, J., Seven, A. B., Prinslow, E. A., Voleti, R., Häussinger, D., Bonvin, A.

613   M. J. J., Tomchick, D. R., Vendruscolo, M., Graham, B., Südhof, T. C., and Rizo, J.:

614   Dynamic binding mode of a synaptotagmin-1-SNARE complex in solution, Nat. Struct.

615   Mol. Biol., 22, 555–564, https://doi.org/10.1038/nsmb.3035, 2015.

616   Bush, K.: Proliferation and significance of clinically relevant β-lactamases, Ann. N. Y. Acad.

617   Sci., 1277, 84−90, https://doi.org/10.1111/nyas.12023, 2013.

618   Bush, K.: Alarming β-lactamase-mediated resistance in multidrug-resistant

619   *Enterobacteriaceae*, Curr. Opin. Microbiol., 13, 558−564,

620   https://doi.org/10.1016/j.mib.2010.09.006, 2010.

621   Carruthers, T. J.: Paramagnetism & Structural Biology: Biochemical & Biophysical Analysis

622   of IMP-1 Metallo-β-lactamase, PhD thesis, The Australian National University, Canberra,

623   221 pp., 2014.

624   Carruthers, T. J., Carr, P. D., Loh, C.-T., Jackson, C. J., and Otting, G.: Fe^{3+} located in the

625   dinuclear metallo-β-lactamase IMP-1 by pseudocontact shifts, Angew. Chemie Int. Ed., 53,

626   14269−14272, https://doi.org/10.1002/anie.201408693, 2014.

627 Chen, W.-N., Nitsche, C., Pilla, K. B., Graham, B., Huber, T., Klein, C. D., and Otting, G.:
628   Sensitive NMR approach for determining the binding mode of tightly binding ligand
629   molecules to protein targets, J. Am. Chem. Soc., 138, 4539−4546,
630   https://doi.org/10.1021/jacs.6b00416, 2016.

631 Concha, N. O., Rasmussen, B. A., Bush, K., and Herzberg, O.: Crystal structure of the wide-
632   spectrum binuclear zinc β-lactamase from *Bacteroides fragilis*, Structure, 4, 823–836,
633   https://doi.org/10.1016/S0969-2126(96)00089-5, 1996.

634 Concha, N. O., Janson, C. A., Rowling, P., Pearson, S., Cheever, C. A., Clarke, B. P., Lewis,
635   C., Galleni, M., Frere, J.-M., Payne, D. J., Bateson, J. H., and Abdel-Meguid, S. S.: Crystal
636   Structure of the IMP-1 metallo-β-lactamase from *Pseudomonas aeruginosa* and its complex
637   with a mercaptocarboxylate inhibitor: binding determinants of a potent, broad-spectrum
638   inhibitor, Biochemistry, 39, 4288–4298, https://doi.org/10.1021/bi992569m, 2000.

639 Crick, D. J., Wang, J. X., Graham, B., Swarbrick, J. D., Mott, H. R., and Nietlispach, D.:
640   Integral membrane protein structure determination using pseudocontact shifts, J. Biomol.
641   NMR, 61, 197–207, https://doi.org/10.1007/s10858-015-9899-6, 2015.

642 de la Cruz, L., Nguyen, T.H.D., Ozawa, K., Shin, J., Graham, B., Huber, T., and Otting, G.:
643   Binding of low-molecular weight inhibitors promotes large conformational changes in the
644   dengue virus NS2B-NS3 protease: fold analysis by pseudocontact shifts, J. Am. Chem. Soc.,
645   133, 19205–19215, https://doi.org/10.1021/ja208435s, 2011.

646 Galleni, M., Lamotte-Brasseur, J., Rossolini, G. M., Spencer, J., Dideberg, O., Frère, J.-M.,
647   and The Metallo-β-Lactamase Working Group: Standard numbering scheme for class B β-
648   lactamases. Antimicrob. Agents Chemother., 45, 660–663,
649   https://doi.org/10.1128/AAC.45.3.660-663.2001, 2001.

650 Gianquinto, E., Tondi, D., D'Arrigo, G., Lazzarato, L., and Spyrakis, F.: Can we exploit β-
651   lactamases intrinsic dynamics for designing more effective inhibitors? Antibiotics, 9, 833,
652   https://doi.org/10.3390/antibiotics9110833, 2020.

653 González, M. M., Abriata, L. A., Tomatis, P. E., and Vila, A. J.: Optimization of
654   conformational dynamics in an epistatic evolutionary trajectory, Mol. Biol. Evol., 33, 1768–
655   1776, https://doi.org/10.1093/molbev/msw052, 2016.

656 Graham, B., Loh, C.T., Swarbrick, J.D., Ung, P., Shin, J., Yagi, H., Jia, X., Chhabra, S.,
657   Pintacuda, G., Huber, T., and Otting, G.: A DOTA-amide lanthanide tag for reliable
658   generation of pseudocontact shifts in protein NMR spectra, Bioconjugate Chem., 22, 2118–
659   2125, https://doi.org/10.1021/bc200353c, 2011.

660   Guan, J. Y., Keizers, P. H. J., Liu, W. M., Löhr, F., Skinner, S. P., Heeneman, E. A., Schwalbe,
661   H., Ubbink, M., and Siegal, G.: Small-molecule binding sites on proteins established by
662   paramagnetic NMR spectroscopy. J. Am. Chem. Soc., 135, 5859–5868,
663   https://doi.org/10.1021/ja401323m, 2013.

664   Herath, I. D., Breen, C., Hewitt, S. H., Berki, T. R., Kassir, A. F., Dodson, C., Judd, M., Jabar,
665   S., Cox, N., Otting, G., and Butler, S. J.: A chiral lanthanide tag for stable and rigid
666   attachment to single cysteine residues in proteins for NMR, EPR and time-resolved
667   luminescence studies, Chem. Eur. J., 27, 13009–13023,
668   https://doi.org/10.1002/chem.202101143, 2021.

669   Hinchliffe, P., González, M. M., Mojica, M. F., González, J. M., Castillo, V., Saiz, C.,
670   Kosmopoulou, M., Tooke, C. L., Llarrull, L. I., Mahler, G., and Bonomo, R. A.: Cross-class
671   metallo-β-lactamase inhibition by bisthiazolidines reveals multiple binding modes, Proc.
672   Nat. Acad. Sci., 113, E3745–E3754, https://doi.org/10.1073/pnas.1601368113, 2016.

673   Hinchliffe, P., Tanner, C. A., Krismanich, A. P., Labbé, G., Goodfellow, V. J., Marrone, L.,
674   Desoky, A. Y., Calvopiña, K., Whittle, E. E., Zeng, F., and Avison, M. B.: Structural and
675   kinetic studies of the potent inhibition of metallo-β-lactamases by 6-
676   phosphonomethylpyridine-2-carboxylates, Biochemistry, 57, 1880–1892,
677   https://doi.org/10.1021/acs.biochem.7b01299, 2018.

678   Hiraiwa, Y., Saito, J., Watanabe, T., Yamada, M., Morinaka, A., Fukushima, T., and Kudo, T.:
679   X-ray crystallographic analysis of IMP-1 metallo-β-lactamase complexed with a 3-
680   aminophthalic acid derivative, structure-based drug design, and synthesis of 3,6-
681   disubstituted phthalic acid derivative inhibitors, Bioorg. Med. Chem. Lett., 24, 4891–4894,
682   https://doi.org/10.1016/j.bmcl.2014.08.039, 2014.

683   Huntley, J.J.A., Scrofani, S.D.B., Osborne, M.J., Wright, P.E., and Dyson, H.J.: Dynamics of
684   the metallo-β-lactamase from *Bacteroides fragilis* in the presence and absence of a tight-
685   binding inhibitor, Biochemistry, 39, 13356–13364, https://doi.org/10.1021/bi001210r,
686   2000.

687   Huntley, J. J. A., Fast, W., Benkovic, S. J., Wright, P. E., and Dyson, H. J.: Role of a solvent-
688   exposed tryptophan in the recognition and binding of antibiotic substrates for a metallo-β-
689   lactamase, Protein Sci., 12, 1368–1375, https://doi.org/10.1110/ps.0305303, 2003.

690   Ito, H., Arakawa, Y., Ohsuka, S., Wachorotayankun, R., Kato, N., and Ohta, M.: Plasmid-
691   mediated dissemination of the metallo-β-lactamase gene *bla*IMP among clinically isolated

692   strains of *Serratia marcescens*, Antimicrob. Agents Chemother., 39, 824–829,
693   https://doi.org/10.1128/AAC.39.4.824, 1995.

694   John, M., Park, A. Y., Pintacuda, G., Dixon, N. E., and Otting, G.: Weak alignment of
695   paramagnetic proteins warrants correction for residual CSA effects in measurements of
696   pseudocontact shifts, J. Am. Chem. Soc., 127, 17190–17191,
697   https://doi.org/10.1021/ja0564259, 2005.

698   John, M., Park, A. Y., Pintacuda, G., Dixon, N. E., and Otting, G.: Weak alignment of
699   paramagnetic proteins warrants correction for residual CSA effects in measurements of
700   pseudocontact shifts, J. Am. Chem. Soc., 127, 17190–17191,
701   https://doi.org/10.1021/ja0564259, 2005.

702   Joss, D., Walliser, R. M., Zimmermann, K., and Häussinger, D.: Conformationally locked
703   lanthanide chelating tags for convenient pseudocontact shift protein nuclear magnetic
704   resonance spectroscopy, J. Biomol. NMR, 72, 29–38, https://doi.org/10.1007/s10858-018-
705   0203-4, 2018.

706   Keizers, P. H. J., Saragliadis, A., Hiruma, Y., Overhand, M., and Ubbink, M.: Design,
707   synthesis, and evaluation of a lanthanide chelating protein probe: CLaNP-5 yields
708   predictable paramagnetic effects independent of environment, J. Am. Chem. Soc., 130,
709   14802–14812, https://doi.org/10.1021/ja8054832, 2008.

710   Keizers, P. H. J., Mersinli, B., Reinle, W., Donauer, J., Hiruma, Y., Hannemann, F., Overhand,
711   M., Bernhardt, R., and Ubbink, M.: A solution model of the complex formed by adrenodoxin
712   and adrenodoxin reductase determined by paramagnetic NMR spectroscopy, Biochemistry,
713   49, 6846–6855, https://doi.org/10.1021/bi100598f, 2010.

714   Kobashigawa, Y., Saio, T., Ushio, M., Sekiguchi, M., Yokochi, M., Ogura, K., and Inagaki, F.:
715   Convenient method for resolving degeneracies due to symmetry of the magnetic
716   susceptibility tensor and its application to pseudo contact shift-based protein-protein
717   complex structure determination, J. Biomol. NMR, 53, 53–63,
718   https://doi.org/10.1007/s10858-012-9623-8, 2012.

719   Laraki, N., Galleni, M., Thamm, I., Riccio, M. L., Amicosante, G., Frère, J.-M., and Rossolini,
720   G. M.: Structure of In101, a *bla*$_{IMP}$-containing *Pseudomonas aeruginosa* integron
721   phyletically related to In5, which carries an unusual array of gene cassettes, Antimicrob.
722   Agents Chemother., 43, 890–901, https://doi.org/10.1128/AAC.43.4.890, 1999a.

723   Laraki, N., Franceschini, N., Rossolini, G. M., Santucci, P., Meunier, C., De Pauw, E.,
724   Amicosante, G., Frère, J.-M., and Galleni, M.: Biochemical characterization of the
725   *Pseudomonas aeruginosa* 101/1477 metallo-β-lactamase IMP-1 produced by *Escherichia*

726 *coli*, Antimicrob. Agents Chemother., 43, 902–906, https://doi.org/10.1128/AAC.43.4.902,
727   1999b.

728 Lescanne, M., Ahuja, P., Blok, A., Timmer, M., Akerud, T., and Ubbink, M.: Methyl group
729   reorientation under ligand binding probed by pseudocontact shifts, J. Biomol. NMR, 71,
730   275–285, https://doi.org/10.1007/s10858-018-0190-5, 2018.

731 Linciano, P., Cendron, L., Gianquinto, E., Spyrakis, F., and Tondi, D.: Ten years with New
732   Delhi metallo-β-lactamase-1 (NDM-1): from structural insights to inhibitor design, ACS
733   Infect. Dis. 5, 9–34, https://doi.org/10.1021/acsinfecdis.8b00247, 2018.

734 Maleckis, A., Herath, I. D., and Otting, G.: Synthesis of $^{13}C/^{19}F/^2H$ labeled indoles for use as
735   tryptophan precursors for protein NMR spectroscopy, Org. Biomol. Chem., 19, 5133–5147,
736   https://doi.org/10.1039/D1OB00611H, 2021.

737 Man, B., Su, X.-C., Liang, H., Simonsen, S., Huber, T., Messerle, B. A., and Otting, G.: 3-
738   Mercapto-2,6-pyridinedicarboxylic acid, a small lanthanide-binding tag for protein studies
739   by NMR spectroscopy, Chem. Eur. J., 16, 3827–3832,
740   https://doi.org/10.1002/chem.200902904, 2010.

741 Markley, J. L., Bax, A., Arata, Y., Hilbers, C. W., Kaptein, R., Sykes, B. D., Wright, P. E., and
742   Wüthrich, K.: Recommendations for the presentation of NMR structures of proteins and
743   nucleic acids - IUPAC-IUBMB-IUPAB Inter-Union Task Group on the Standardization of
744   Data Bases of Protein and Nucleic Acid Structures Determined by NMR Spectroscopy, J.
745   Biomol. NMR, 12, 1–23, https://doi.org/10.1023/A:1008290618449, 1998.

746 Meissner, A., Duus, J. Ø., and Sørensen, O. W.: Spin-state-selective excitation. Application for
747   E.COSY-type measurement of J_{HH} coupling constants, J. Magn. Reson., 128, 92–97,
748   https://doi.org/10.1006/jmre.1997.1213, 1997.

749 Moali, C., Anne, C., Lamotte-Brasseur, J., Groslambert, S., Devreese, B., Van Beeumen, J.,
750   Galleni, M., and Frère, J.M.: Analysis of the importance of the metallo-β-lactamase active
751   site loop in substrate binding and catalysis, Chemistry & Biology, 10, 319–329,
752   https://doi.org/10.1016/S1074-5521(03)00070-X, 2003.

753 Orton, H. W., Huber, T., and Otting, G.: Paramagpy: software for fitting magnetic
754   susceptibility tensors using paramagnetic effects measured in NMR spectra, Magn.
755   Reson., 1, 1–12, https://doi.org/10.5194/mr-1-1-2020, 2020.

756 Palacios, A. R, Mojica, M. F., Giannini, E., Taracila, M. A., Bethel, C. R., Alzari, P. M., Otero,
757   L. H., Klinke, S., Llarrull, L. I., Bonomo, R. A., and Vila, A. J.: The reaction mechanism of
758   metallo-β-lactamases is tuned by the conformation of an active-site mobile loop,

Antimicrob. Agents Chemother, 63, e01754-18, https://doi.org/10.1128/AAC.01754-18, 2019.

Payne, D. J., Hueso-Rodriguez, J. A., Boyd, H., Concha, N. O., Janson, C. A., Gilpin, M., Bateson, J. H., Cheever, C., Niconovich, N. L., Pearson, S., Rittenhouse, S., Tew, D., Díez, E., Pérez, P., de la Fuente, J., Rees, M., and Rivera-Sagredo, A.: Identification of a series of tricyclic natural products as potent broad-spectrum inhibitors of metallo-β-lactamases, Antimicrob. Agents Chemother., 46, 1880–1886, https://doi.org/10.1128/AAC.46.6.1880-1886.2002, 2002.

Pearce, B. J. G., Jabar, S., Loh, C. T., Szabo, M., Graham, B., and Otting, G.: Structure restraints from heteronuclear pseudocontact shifts generated by lanthanide tags at two different sites, J. Biomol. NMR, 68, 19–32, https://doi.org/10.1007/s10858-017-0111-z, 2017.

Pilla, K. B., Otting, G., and Huber, T.: Protein structure determination by assembling super-secondary structure motifs using pseudocontact shifts, Structure, 25, 559–568, https://doi.org/10.1016/j.str.2017.01.011, 2017.

Pintacuda, G., Park, A. Y., Keniry, M. A., Dixon, N. E., and Otting, G.: Lanthanide labeling offers fast NMR approach to 3D structure determinations of protein-protein complexes, J. Am. Chem. Soc., 128, 3696–3702, https://doi.org/10.1021/ja057008z, 2006.

Rossi, M.-A., Martinez, V., Hinchliffe, P., Mojica, M. F., Castillo, V., Moreno, D. M., Smith, R., Spellberg, B., Drusano, G. L., Banchio, C., Bonomo, R. A., Spencer, J., Vila, A. J., and Mahler, G.: 2-Mercaptomethyl-thiazolidines use conserved aromatic–S interactions to achieve broad-range inhibition of metallo-β-lactamases, Chem. Sci., 12, 2898–2908, https://doi.org/10.1039/d0sc05172a, 2021.

Salimraj, R., Hinchliffe, P., Kosmopoulou, M., Tyrrell, J. M., Brem, J., van Berkel, S. S., Verma, A., Owens, R. J., McDonough, M. A., Walsh, T. R., Schofield, C. J., and Spencer, J.: Crystal structures of VIM-1 complexes explain active site heterogeneity in VIM-class metallo-β-lactamases, FEBS J., 286, 169–183, https://doi.org/10.1111/febs.14695, 2018.

Shishmarev, D. and Otting, G.: How reliable are pseudocontact shifts induced in proteins and ligands by mobile paramagnetic metal tags? A modelling study, J. Biomol. NMR, 56, 203–216, https://doi.org/10.1007/s10858-013-9738-6, 2013.

Softley, C. A., Zak, K. M., Bostock, M. J., Fino, R., Zhou, R. X., Kolonko, M., Mejdi-Nitiu, R., Meyer, H., Sattler, M., and Popowicz, G. M.: Structure and molecular recognition

791   mechanism of IMP-13 metallo-β-lactamase, Antimicrob. Agents Chemother., 64, e00123-
792   20, https://doi.org/10.1128/AAC.00123-20, 2020.

793 Su, X.-C., McAndrew, K., Huber, T., and Otting, G.: Lanthanide-binding peptides for NMR
794   measurements of residual dipolar couplings and paramagnetic effects from multiple angles,
795   J. Am. Chem. Soc., 130, 1681–1687, https://doi.org/10.1021/ja076564l, 2008.

796 Toney, J. H., Hammond, G. G., Fitzgerald, P. M., Sharma, N., Balkovec, J. M., Rouen, G. P.,
797   Olson, S. H., Hammond, M. L., Greenlee, M. L., and Gao, Y. D.: Succinic acids as potent
798   inhibitors of plasmid-borne IMP-1 metallo-β-lactamase, J. Biol. Chem., 276, 31913–31918,
799   https://doi.org/10.1074/jbc.M104742200, 2001.

800 van Duin, D., Kaye, K. S., Neuner, E. A., and Bonomo, R. A.: Carbapenem-resistant
801   Enterobacteriaceae: a review of treatment and outcomes, Diagn. Microbiol. Infect. Dis. 75,
802   115−120, https://doi.org/10.1016/j.diagmicrobio.2012.11.009, 2013.

803 Wachino, J., Kanechi, R., Nishino, E., Mochizuki, M., Jin, W., Kimura, K., Kurosaki, H., and
804   Arakawa, Y.: 4-Amino-2-sulfanylbenzoic acid as a potent subclass B3 metallo-β-lactamase-
805   specific inhibitor applicable for distinguishing metallo-β-lactamase subclasses, Antimicrob.
806   Agents Chemother. 63, e01197-19, https://doi.org/10.1128/AAC.01197-19, 2019.

807 Watanabe, M., S. Iyobe, M. Inoue, and S. Mitsuhashi: Transferable imipenem resistance in
808   *Pseudomonas aeruginosa*, Antimicrob. Agents Chemother. 35, 147–151, https://doi.org/
809   10.1128/AAC.35.1.147, https://doi.org/10.1128/AAC.35.1.147, 1991.

810 Yagi, H., Pilla, K. B., Maleckis, A., Graham, B., Huber, T., and Otting, G.: Three-dimensional
811   protein fold determination from backbone amide pseudocontact shifts generated by
812   lanthanide tags at multiple sites, Structure, 21, 883–890,
813   https://doi.org/10.1016/j.str.2013.04.001, 2013.

814 Yamaguchi, Y., Matsueda, S., Matsunaga, K., Takashio, N., Toma-Fukai, S., Yamagata, Y.,
815   Shibata, N., Wachino, J., Shibayama, K., Arakawa, Y., and Kurosaki, H.: Crystal structure
816   of IMP-2 metallo-β-lactamase from *Acinetobacter* spp.: comparison of active-site loop
817   structures between IMP-1 and IMP-2, Biol. Pharm. Bull. 38, 96–
818   101, https://doi.org/10.1248/bpb.b14-00594, 2015.

819 Yamaguchi, Y., Kato, K., Ichimaru, Y., Jin, W., Sakai, M., Abe, M., Wachino, J., Arakawa,
820   Y., Miyagi, Y., Imai, M., Fukuishi, N., Yamagata, Y., Otsuka, M., Fujita, M., and Kurosaki,
821   H.: Crystal structures of metallo-β-lactamase (IMP-1) and its D120E mutant in complexes
822   with citrate and the inhibitory effect of the benzyl group in citrate monobenzyl ester, J. Med.
823   Chem., 64, 10019–10026, https://doi.org/10.1021/acs.jmedchem.1c00308, 2021.

824   Yamaguchi, H., M. Nukaya, and T. Sawai, T: Sequence of *Klebsiella pneumoniae* RDK4

825   metallo-β-lactamase, EMBO database accession no. D29636, EMBO, Heidelberg,

826   Germany, 1994.

827   Zimmermann, K., Joss, D., Müntener, T., Nogueira, E. S., Schäfer, M., Knörr, L., Monnard,

828   F. W., and Häussinger, D.: Localization of ligands within human carbonic anhydrase II

829   using ^{19}F pseudocontact shift analysis, Chem. Sci., 10, 5064–5072,

830   https://doi.org/10.1039/c8sc05683h, 2019.